arXiv:astro-ph/0101299v1 17 Jan 2001

Chandra Observations of the X-Ray Jet of 3C 273

Rita M. Sambruna

George Mason University, Dept. of Physics & Astronomy and School of Computational Sciences, 4400 University Drive, M/S 3F3, Fairfax, VA 22030

C. Megan Urry

STScI, 3700 San Martin Dr., Baltimore 21218, MD

F. Tavecchio and L. Maraschi

Osservatorio Astronomico di Brera, via Brera 28, 20121 Milano, Italy

R. Scarpa

STScI, 3700 San Martin Dr., Baltimore 21218, MD

G. Chartas

The Pennsylvania State University, Department of Astronomy and Astrophysics, 525 Davey Lab, State College, PA 16802

T. Muxlow

Jodrell Bank Observatory, University of Manchester, Macclesfield, Cheshire, SK11 9DL, UK

Received _____; accepted _____

ABSTRACT

We report results from *Chandra* observations of the X-ray jet of 3C 273 during the calibration phase in 2000 January. The zeroeth-order images and spectra from two 40-ks exposures with the HETG and LETG+ACIS-S show a complex X-ray structure. The brightest optical knots are detected and resolved in the 0.2–8 keV energy band. The X-ray morphology tracks well the optical. However, while the X-ray brightness decreases along the jet, the outer parts of the jet tend to be increasingly bright with increasing wavelength. The spectral energy distributions of four selected regions can best be explained by inverse Compton scattering of (beamed) cosmic microwave background photons. The model parameters are compatible with equipartition and a moderate Doppler factor, which is consistent with the one-sidedness of the jet. Alternative models either imply implausible physical conditions and energetics (the synchrotron self-Compton model) or are sufficiently ad hoc to be unconstrained by the present data (synchrotron radiation from a spatially or temporally distinct particle population).

Subject Headings: galaxies: active — galaxies: jets — (galaxies:) quasars: individual (3C273) — X-rays: galaxies

1. Introduction

Being nearby ($z = 0.158$), the jet of 3C 273 is ideal for intensive multiwavelength studies. The 10″-long radio jet has a knotty morphology, with the first detected knot at $\sim 13''$ from the core and increasing radio intensity toward a terminal bright hot spot $\sim 22''$ from the core (Flatters & Conway 1985). Variable radio polarization and low Faraday rotation have been observed along the jet (Conway et al. 1993). In the near-infrared, the jet brightness tracks well the radio, while at optical wavelengths the jet is much narrower and concentrated along the axis (Röser & Meisenheimer 1991; Bahcall et al. 1995; Neumann, Meiseinheimer, & Röser 1997). This is globally consistent with synchrotron emission being the dominant mechanism from radio through optical.

On much smaller (VLBI) scales, 3C 273 has a radio jet with superluminal components (Davis, Muxlow, & Unwin 1991), implying bulk relativistic motion of the emitting plasma, with a jet-to-counterjet ratio of 5300. The resulting Doppler beaming provides a natural explanation for the absence of a visible counterjet. On kiloparsec scales, the X-ray/optical emission remains asymmetric, suggesting relativistic bulk motion may still be present on large scales.

In the X-rays, the 3C 273 jet was first detected with *Einstein* and *ROSAT* (Harris & Stern 1987; Röser et al. 2000), with most of the X-ray flux coming from the brightest optical knot. The spectral energy distributions from radio to X-rays of the individual knots, resolved at the *ROSAT* HRI resolution ($\sim 15''$), show a variety of shapes. For the brightest knot, the X-ray flux appeared to lie on the extrapolation from the radio-optical spectrum, suggesting synchrotron emission could extend to at least 2 keV. For the remaining knots, the X-rays were above the extrapolation from the longer wavelengths (Röser et al. 2000).

Here we use the *Chandra* ACIS-S observation of the 3C 273 jet obtained during the calibration phase (80 ks exposure total) to study the jet morphology in greater detail. The

Chandra data are compared to observations at longer wavelengths using archival *HST* U- and R-band data and deep *MERLIN* observations at 1.65 GHz. Throughout this work we adopt $H_0 = 75$ km/s/Mpc and $q_0 = 0.5$, so at the distance of 3C 273, $1''$=2.4 kpc.

2. Observations and Data Analysis

Chandra observed 3C 273 during the calibration phase in January 2000, with ACIS-S (Garmire et al. 2000) plus the Low Energy Transmission Grating (LETG) for 40 ks on January 9–10, and with ACIS-S plus the High Energy Transmission Grating (HETG) for 40 ks on January 10. Here we concentrate on the zeroeth-order (undispersed) HETG and LETG images of the jet. After screening out data corresponding to bad aspect times and grades, 39.8 ks were left in the LETG and 39.4 ks in the HETG exposures, which were gain corrected using the appropriate files for the dates of observation. The S3 background was stable during both observations. Images were extracted in the energy range 0.2–8 keV, where the background is lower ($\sim 8.6 \times 10^{-6}$ c s^{-1} arcsec^{-2} for LETG, $\sim 5.1 \times 10^{-6}$ c s^{-1} arcsec^{-2} for HETG). We also accumulated separately soft (0.2–1 keV) and hard (1–8 keV) images calibrated in flux, in order to study spectral evolution along the jet.

To maximize the spatial resolution in the final image, we deconvolved the data using the maximum likelihood algorithm, following Chartas et al. (2000). The HETG and LETG images were deconvolved separately, then stacked together. The effective resolution (FWHM) of the deconvolved X-ray images is $0.37''$ FWHM. However, fluxes were extracted from the original, un-deconvolved event files.

For X-ray spectral analysis only the ACIS-S HETG zeroeth-order image was used since the ACIS+LETG configuration is not as well calibrated yet. Position-dependent responses and ancillary files were created, and spectra were rebinned to have at least 20 counts per

bin, to validate the use of the χ^2 statistic. Analysis of calibration HETG observations of Capella and simulations with `MARX` v.3.0 show that the contribution of the core PSF wings is negligible (less than 1 count/bin) at $\sim 13''$ or more from the core, where the first bright jet knot is detected. Because of the roll angle, the jet X-ray emission is unaffected by the grating diffraction spikes in both the HETG and LETG data.

HST images of 3C 273 obtained in the R and U bands (first reported by Röser et al. 1997) and *MERLIN* data at 1.65 GHz (first reported by Bahcall et al. 1995) were reanalyzed in order to extract spectra in apertures matched to those used in the X-rays. The resolution of the *MERLIN* data consists of a beamwidth $0.18''$x $0.14''$ FWHM at a position angle of 27 deg (Bahcall et al. 1995). The final radio-optical-X-ray spectra of the jet knots are therefore accurate representations of the spectra of the X-ray-emitting regions. The radial profiles at all wavelengths were extracted by running a $1''$ slice orthogonally to the jet axis. The resolution of the radio and optical data is $0.16''$/pixel and $0.046''$/pixel, respectively.

3. Results

3.1. X-Ray, Optical, and Radio Morphologies of Jet

Figure 1 shows the *Chandra* ACIS-S image of the 3C 273 jet in the 0.2–8 keV band. The X-ray jet is $\sim 8''$-long and has a knotty morphology, starting with a bright, resolved knot at $\sim 13''$ from the core, coincident with optical knot A1 (using notation from Bahcall et al. 1995). This is followed by a second bright knot at $\sim 15''$, coincident with optical knot B1, with weak X-ray emission in between. The X-ray emission then fades to a low but still detectable level before terminating at knot D. No X-ray emission was detected between the nucleus and knot A1. A total of 1361 counts were detected from the jet in the 0.2–8 keV

band (614 from the HETG, 747 from the LETG), of which 584 are contained in the first knot A1 within 0.9″.

Figures 2a–d shows the jet surface brightness profiles at X-ray, optical (U and R bands) and radio (1.65 GHz) wavelengths, normalized to the peak intensity in each band. Nearly all the optical and radio knots are detected at X-rays, the exception being the final hot spot (called "H" by Bahcall et al. 1995) at $\sim 21.5''$, which is bright in the radio and optical but has no obvious X-ray counterpart. The peaks align to within a few tenths of an arcsec, well within the astrometric and attitude accuracies of *Chandra* and *HST*. The four normalized profiles show that, while the X-ray brightness decreases along the jet, at longer wavelengths the outer parts of the jet become increasingly dominant. Note that this behaviour appears rather regular through the U and R bands down to the radio.

3.2. Spectral Energy Distributions

We constructed radio-to-X-ray Spectral Energy Distributions (SEDs) for four interesting regions along the jet, identified in the *Chandra* profile in Figure 2 as A, B, C, and D. Fluxes at X-ray, optical, and radio wavelengths were extracted from circles positioned at the centers of these regions and with radii equal to half the marked size. Region A corresponds to knot A1 (maximum X-ray flux); region B encloses optical knots A2, B1, and B2; region C includes knots C1–C3; and region D contains knots D1–D3. The X-ray fluxes were corrected for absorption using a column density equal to the Galactic value, $N_H = 1.8 \times 10^{20}$ cm^{-2} (Elvis et al. 1989), which is consistent with the X-ray spectrum of knot A1 and the optical fluxes were dereddened assuming A_V=0.1.

Figure 3 shows the SEDs of the four regions of the jet. In all cases, the X-ray flux lies above the extrapolation from the radio-to-optical continuum, which steepens in the

optical band. Thus the X-rays appear to belong to a distinct spectral component. The radio-to-optical flux ratio increases from the inner to the outer parts, in accordance with the steepening of the optical continuum (e.g., Röser & Meisenheimer 1991). The X-ray spectrum of region A in the energy range 2–8 keV was fitted by a power law with photon index $\Gamma_x = 2.1^{+0.5}_{-0.3}$ (90% confidence interval) and Galactic absorption. Region B has a similar X-ray spectrum but larger errors due to the lower flux, and there are too few photons for spectral analysis in the remaining regions. We can not set constraints on the low-energy ($\lesssim 1$ keV) spectrum given the current calibration uncertainties.

From the hardness ratio, HR=1–8 keV/0.2–1 keV, there is a slight indication of spectral softening along the jet, but only at the 2 sigma level: HR=1.2 ± 0.1 for region A and HR=0.9 ± 0.2 for region D (using uncertainties as prescribed by Gehrels 1986). With better statistics, we could determine whether this effect is real.

4. Discussion: The Multiwavelength Jet Spectra

While the radio-through-optical spectrum from the 3C 273 jet is almost certainly due to synchrotron radiation (see § 1), the X-rays can not be attributed to synchrotron emission from the same population of electrons, since this would be inconsistent with the shape of the SEDs in Figure 3, except possibly for region A (and with the different jet morphologies in Figure 2). We conclude that in all four regions the X-rays arise from a different spectral component than does the radio-optical emission.

We considered the following possibilities for the origin of the X-rays: (1) synchrotron emission from a second, much more energetic population of electrons (Röser et al. 2000); (2) inverse Compton scattering of radio-optical synchrotron photons; (3) inverse Compton scattering of photons external to the jet. We can rule out a fourth possibility, that the

0.8–2 keV X-rays are bremmstrahlung from thermal gas confining the radio-optical jet, since the required density is higher than allowed by the observed (low) rotation measure (Conway et al. 1993); such a model is also inconsistent with the X-ray spectrum of knot A and with the general morphological correspondence of X-ray and radio-optical (synchrotron) emission. The present data do not constrain the presence of thermal gas cooler than ~ 1 keV.

4.1. Synchrotron Emission from Two Populations of Electrons

If the second electron population is co-spatial with the first, it must arise from a separate episode of acceleration (since cooling would create a spectrum extending smoothly to lower energies). Its mean electron energy must also be higher (for the same magnetic field), and the acceleration event must have occurred more recently (the electrons not yet having cooled substantially). One possibility is that hotter electrons are produced via proton-induced cascades (Mannheim & Biermann 1992); this model is not constrained by the limited spectral data discussed here.

A simple homogeneous synchrotron model fits the radio-optical emission of the four regions with plausible parameters: B between 1 and 10 μGauss, Doppler factor $\delta \sim 5$, size $\sim 5 \times 10^{21}$ cm, and electron cutoff energies $\gamma_{\rm min} \sim 10$ and $\gamma_{\rm max} \sim 10^6$. For the same magnetic field, X-ray-emitting electrons would have to have $\gamma_{\rm min}$ in the range 10^{6-7} while $\gamma_{\rm max}$ is unconstrained as we do not know the upper-cutoff frequency of the spectrum. The energy distribution of this second population would have a shape similar to the radio-optical-emitting electrons (index 2.6). Alternatively, the second electron population could occupy a distinct region in the jet, with a different magnetic field, in which case there are enough free parameters that the physical state of the jet is essentially not constrained by the present observations.

4.2. Synchrotron Self-Compton (SSC) Emission

X-rays are inevitably produced by synchrotron self-Compton emission, meaning inverse Compton scattering of the radio-optical synchrotron photons by the electrons that emit them. This model can be significantly constrained by a few observed fluxes, at least in the homogeneous approximation (Tavecchio, Maraschi & Ghisellini 1998). However, the only way for the Compton component to be more luminous than the synchrotron component (as is the case in regions A–C; Fig. 3) is if the observed emission is weakly beamed or de-beamed ($\delta \lesssim 1$) which enhances the estimate of the intrinsic photon density. For $\delta \simeq 1$ one needs additionally a very low magnetic field ($B \lesssim 10^{-6}$ G), orders of magnitude below the equipartition value (see the discussion for the case of PKS 0637–752; Tavecchio et al. 2000). A more plausible value of the magnetic field can be recovered if the jet is significantly debeamed ($B \simeq 10^{-5} - 10^{-4}$ G for $\delta \simeq 0.5 - 0.3$). This implies much larger total jet power and is energetically less favorable. It also implies the jet is misaligned, which is implausible given the blazar-like core radio source. Instead, if applicable on large scale, the jet-to-counterjet ratio of 5300 implies a bulk Lorentz factor $\Gamma_{\rm bulk} > 3$ and viewing angle $\theta < 18$, or $\delta > 6$ (for $\alpha = 0.5$). Thus, while SSC emission must be produced, for plausible assumptions it is insufficient to explain the observed X-rays.

4.3. External Compton Emission

X-rays can be produced when relativistic electrons in the jet inverse Compton scatter photons external to the jet (external Compton, or EC). Because the jet is far from the nuclear region, however, the energy density of ambient photons is negligible unless the jet is still relativistic on kiloparsec scales. In that case, the (forward) cosmic microwave background (CMB) photons are beamed in the jet frame, so their intrinsically low rest-frame energy density, 7×10^{-13} ergs s^{-1}, is enhanced by the factor $\Gamma^2_{\rm bulk}$ (Tavecchio et al. 2000).

The EC/CMB model is as fully specified as the SSC model, so similar constraints on B and δ apply (Tavecchio et al. 2000). In this case, however, the model needs a significant beaming factor ($\delta \sim 5$) and can be reasonably close to an equipartition of energy between magnetic field and electrons ($B \sim 10^{-5}$ G). A model SED for knot A is shown in Fig. 3.

The observed decreasing trend of the X-ray/radio luminosity ratio along the jet finds no obvious explanation in any of the scenarios discussed above. Ad hoc variations of the involved parameters must be invoked. Within the EC/CMB scenario the ratio of magnetic to photon energy density in the jet can increase because either the magnetic field increases or the amplification factor for the CMB energy density as seen in the jet ($\Gamma^2_{\rm bulk}$) decreases, or both. In Fig. 3 we show a model SED for knot C, obtained by increasing only the magnetic field by a factor $\simeq 4$ with respect to knot A together with a model SED for knot D obtained increasing B by a further factor of 2 and decreasing Γ by a factor $\simeq 4$ which leaves δ almost constant. The precise values of the parameters used are given in the figure Caption. An enhancement of the magnetic field by compression, as the plasma in the jet goes through successive shocks, is plausible as indicated by polarization maps (Conway et al. 1993). Deceleration at shocks is also plausible just before the main radio hot spot, at which deceleration is presumably so strong (e.g., Röser, Conway, & Meisenheimer 1996), as to drastically suppress X-rays from inverse Compton scattering of CMB photons.

In the EC/CMB model the X-ray emission is produced by electrons of relatively low energy ($\gamma \sim 1000$) (whose spectrum is measurable in the radio). Therefore the cooling timescale is long, implying that a spctral steepening along the jet can not be due to cooling.

Electron cooling also cannot explain the observed knottiness of the X-ray jet which could be due to compression of particles and fields associated with shocks. Alternatively the front of the relativistic plasma may describe a helix around the jet and thus have different angles with respect to the line of sight (even if fixed Lorentz factor). This is consistent with

the optical morphology in the *HST* images, which show a "corkscrew" jet (Bahcall et al. 1995). The X-rays would then be brightest where the alignment was favorable. The physics derived here would be unchanged.

While in our model X-ray emitting electrons have long cooling times, electrons emitting synchrotron optical radiation (close to γ_{max}) cool in a time short compared to the travel time along the jet; the cooling time at knot A is $\sim 5 \times 10^{10}$ s, corresponding to a distance of less then a few kpc. These electrons must therefore be accelerated in situ. From our spectral fits the maximum electron Lorentz factor γ_{max} appears to decrease along the jet (see parameters in Fig. 3 caption). This could be understood as an overall cooling of the accelerated electrons or as a decrease in the efficiency of shock acceleration or a combination of both.

5. Conclusions

We have analyzed the multiwavelength jet in 3C 273, in an attempt to determine its physical state. Of the possible mechanisms for the X-ray emission, the most plausible is inverse Compton scattering of microwave background photons (EC/CMB), which are seen as beamed by jet electrons if there is bulk relativistic motion on kiloparsec scales. The contribution from SSC X-rays is much smaller unless the magnetic field is well below equipartition and/or the observed emission is de-beamed, either of which increases the required jet power to uncomfortable levels. An alternative picture, in which the X-rays come from direct synchrotron radiation, posits a second, distinct population of electrons, which might be produced in a second region (unresolved by the X-ray data) more recently than the cooler population responsible for the radio-optical spectrum. This is a somewhat *ad hoc* model which can not be well constrained given the large number of free parameters. Future longer *Chandra* observations of the 3C 273 jet could provide more sensitive constraints both

spatially and spectrally.

This work was partially supported by NASA grants NAG5–7925 (RMS), NAG5–9327 (CMU, FT, LM), the Italian MURST (MURST-COFIN-98-02-15-41) and ASI (ASI-ARS-98-74 and ASI-I/R/105/00) and from the European Commission (ERBFMRX-CT98-0195). Support was also provided by NASA through grants GO-06363.01-95A and GO-07893.01-96A from STScI, operated by AURA, Inc., under NASA contract NAS 5-26555. *MERLIN* is a national facility operated by the University of Manchester on behalf of PPARC in the UK.

REFERENCES

Bahcall, J. N. et al. 1995, ApJ, 452, L91

Chartas, G. et al. 2000, ApJ, in press (astro-ph/0005227)

Conway, R. G., Garrington, S. T., Perley, R. A., & Biretta, J. A. 1993, A&A, 267, 347

Davis, R.J., Muxlow, T.W.B., & Unwin, S.C. 1991, Nature, 354, 374

Elvis, M., Wilkes, B.J., & Lockman, F. 1989, AJ, 97, 777

Flatters, C. & Conway, R.G. 1985, Nature, 314, 425

Garmire, G. et al. 2000, ApJS, submitted

Gehrels, N. 1986, ApJ, 303, 336

Harris, D. E. & Stern, C. P. 1987, ApJ, 313, 136

Mannheim, K., & Biermann, P. L. 1992, A&A, 253, L21

Neumann, M., Meiseinheimer, K., & Röser, H.-J. 1997, A&A, 326, 69

Röser, H.-J., Meisenheimer, K., Neumann, M., Conway, R. G., & Perley, R. A. 2000, A&A, 360, 99

Röser, H.-J., Meisenheimer, K., Neumann, M., Conway, R. G., Davis, R.J., & Perley, R. A. 1997, Reviews in Modern Astronomy, 10, 253

Röser, H.-J., Conway, R. G., & Meisenheimer, K. 1996, A&A, 314, 414

Röser, H.-J. & Meisenheimer, K. 1991, A&A, 252, 458

Tavecchio, F., Maraschi, L., Sambruna, R.M., & Urry, C.M. 2000, ApJL, submitted

Tavecchio, F., Maraschi, L., & Ghisellini, G. 1998, ApJ, 509, 608

von Montigny, C. et al. 1997, ApJ, 483, 161

This manuscript was prepared with the AAS LaTeX macros v4.0.

Figure 1: *Chandra* ACIS-S image of the jet of 3C 273 (color scale with superimposed contours), from combining two exposures obtained during the calibration phase in 2000 January, for a total exposure of 79.2 ks. A maximum likelihood algorithm was applied to the stacked image (Chartas et al. 2000), yielding a pixel size of 0.125″/pixel and an effective resolution at FWHM of 0.37″. A total of 1361 counts were detected from 0.2–8 keV. The nucleus of 3C 273 is 13″ from this knot, well outside the figure.

Figure 2: Multiwavelength surface brightness profiles along the jet, normalized to the brightest peak in each band. X-ray data from *Chandra*, U- and R-band data from archival *HST* images, and radio data at 1.65 GHz from *MERLIN* observations. The dashed line in the bottom panel show the radio profile multiplied by 10, in order to show the jet structure at radii $\lesssim 20''$. Regions extracted for subsequent spectral analysis are marked A–D at the top. The normalization factors are: 87.2734 counts/bin for the X-rays, 0.17 μJy/pixel for the U band, 0.38 μJy/pixel for the R band, and 0.37 Jy/pixel for the radio.

Figure 3: Spectral energy distributions for regions A, B, C, and D (defined in Fig. 2), extracted from the *MERLIN*, *HST*, and *Chandra* images using matching apertures fixed by the X-ray resolution. The uncertainties on the X-ray fluxes are 40%, while the optical and radio data have 10% uncertainties. The solid lines represent fits to the spectra with the EC/CMB model (see text), with the following parameters: *A:* minimum and maximum electron energy $\gamma_{min} = 20$, $\gamma_{max} = 6 \times 10^6$, index $n = 2.6$, density $K = 8.1 \times 10^{-3}$ cm^{-3}, magnetic field $B = 1.9 \times 10^{-6}$ G, region size $R = 5 \times 10^{21}$ cm, Doppler factor $\delta = 5.2$; *B:* like A, except $\gamma_{max} = 3 \times 10^6$ and $B = 3.6 \times 10^{-6}$ G; *C:* like A, except $\gamma_{max} = 1.5 \times 10^6$ and $B = 8.8 \times 10^{-6}$ G; *D:* like A, except $\gamma_{max} = 7 \times 10^5$, $B = 2.2 \times 10^{-5}$ G, and $\delta = 4.2$.

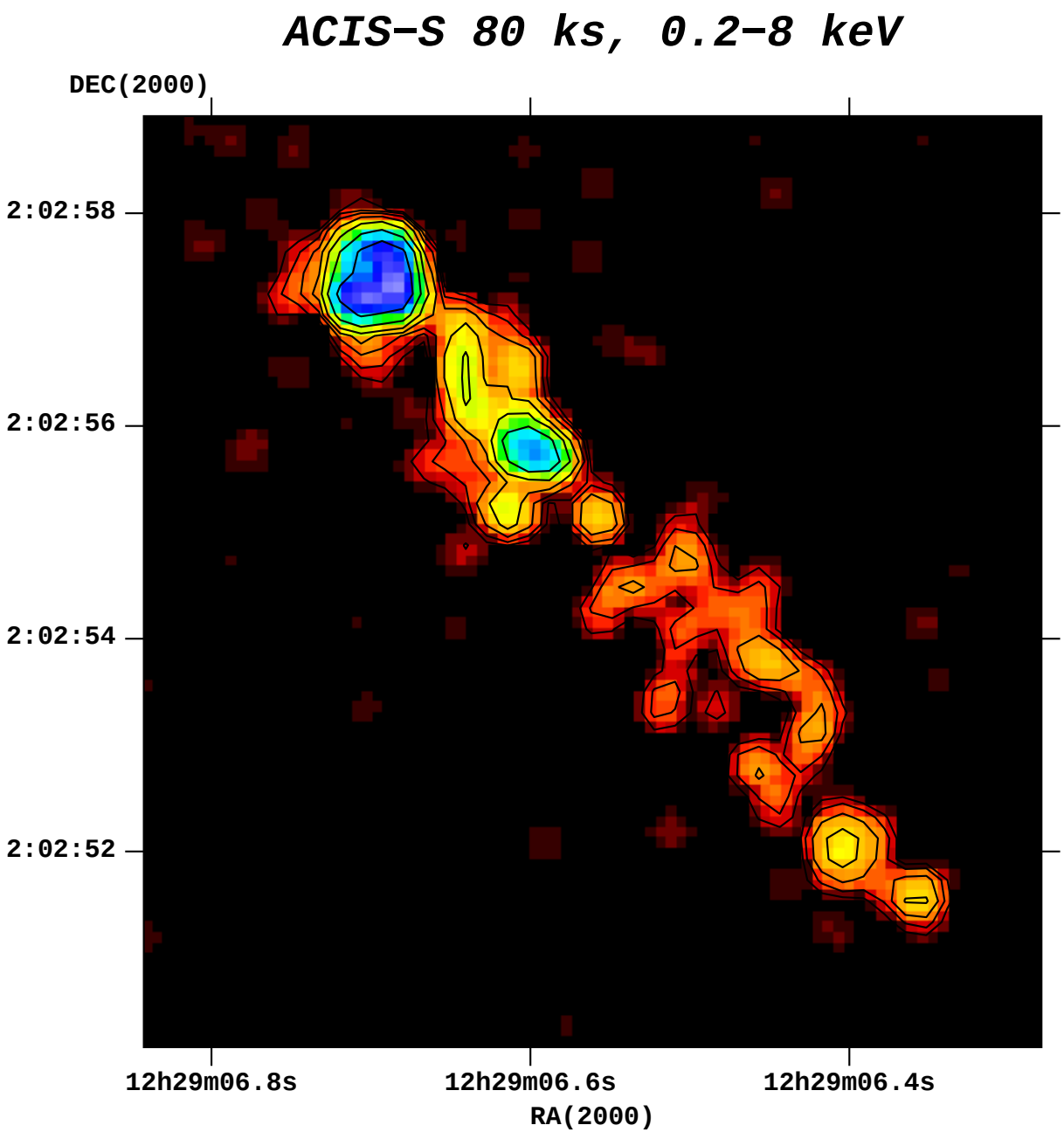
ACIS–S 80 ks, 0.2–8 keV
DEC(2000)
2:02:58
2:02:56
2:02:54
2:02:52
12h29m06.8s
12h29m06.6s
12h29m06.4s
RA(2000)

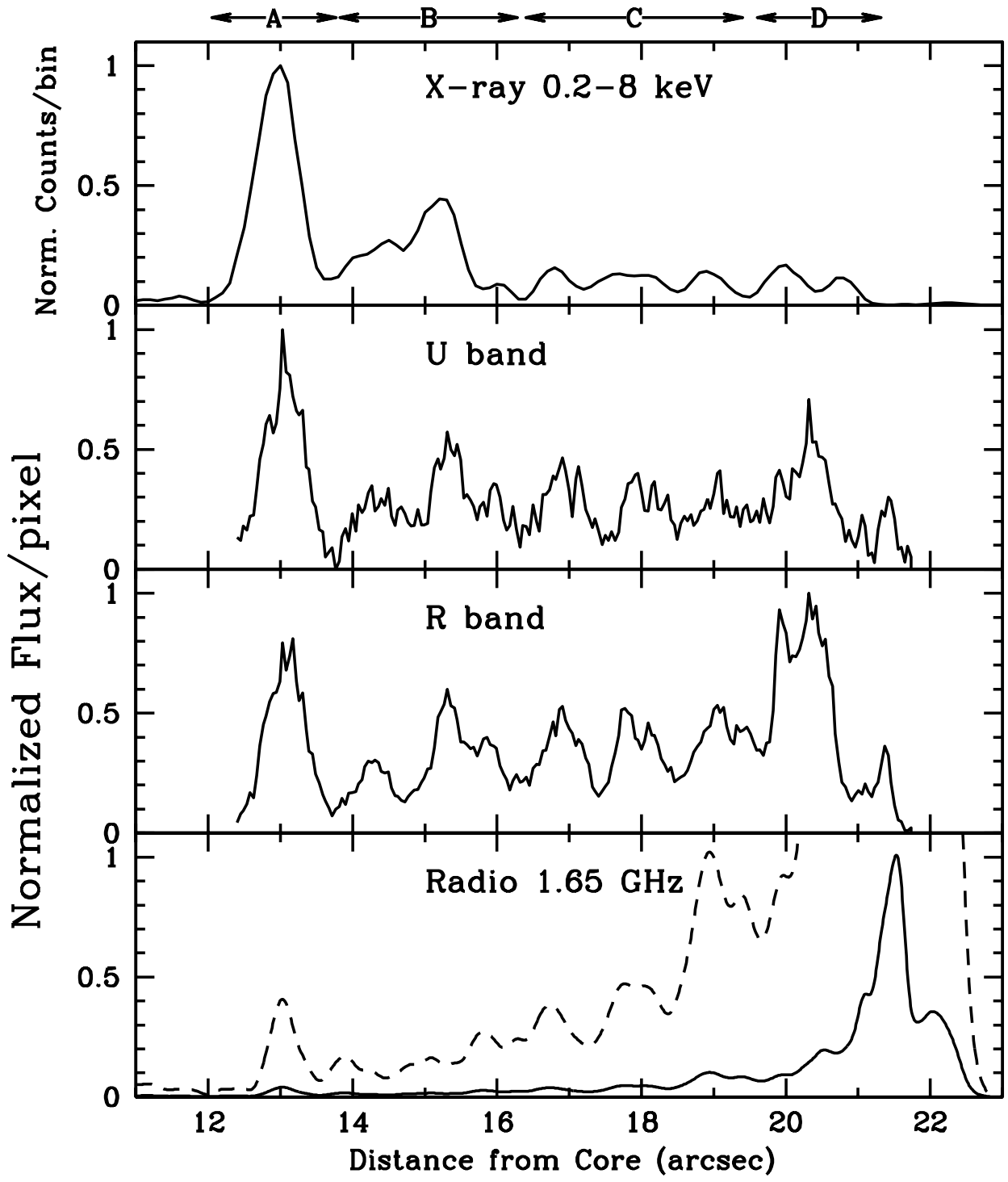
A
B
C
D
X-ray 0.2-8 keV
U band
R band
Radio 1.65 GHz
Norm. Counts/bin
Normalized Flux/pixel
Distance from Core (arcsec)
0
0.5
1
12
14
16
18
20
22

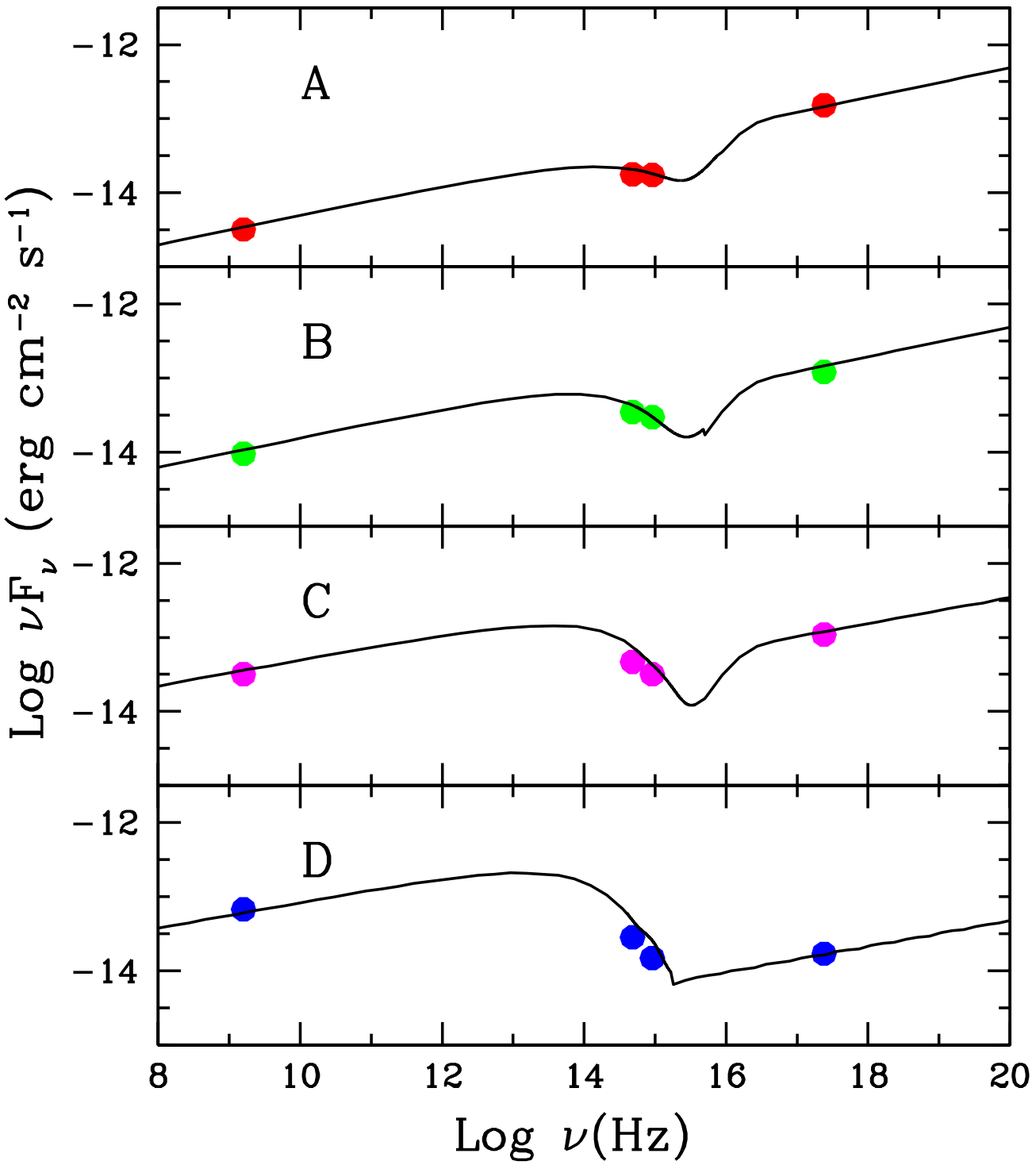
A
B
C
D
−12
−14
Log νF_ν (erg cm^−2 s^−1)
8
10
12
14
16
18
20
Log ν(Hz)